Isolation and structure of the fibril protein, a major component of the internal ribbon for *Spiroplasma* swimming

Yuya Sasajima[1], Takayuki Kato[2], Tomoko Miyata[3], Akihiro Kawamoto[3], Keiichi Namba[3,4,5] and Makoto Miyata[1,6*]

[1]Graduate School of Science, Osaka Metropolitan University, Osaka, Japan

[2]Institute for Protein Research, Osaka University, 3-2 Yamadaoka, Suita, Osaka, Japan

[3]Graduate School of Frontier Biosciences, Osaka University, 1-3 Yamadaoka, Suita, Osaka, Japan

[4]RIKEN Center for Biosystems Dynamics Research and Spring-8 Center, 1-3 Yamadaoka, Suita, Osaka, Japan

[5]JEOL YOKOGUSHI Research Alliance Laboratories, Osaka University, 1-3 Yamadaoka, Suita, Osaka, Japan

[6]The OCU Advanced Research Institute for Natural Science and Technology (OCARINA), Osaka Metropolitan University, Osaka, Japan.

***Correspondence:**

Makoto Miyata

miyata@omu.ac.jp

Keywords: Helical shape, Motility, Cytoskeleton, Filament, Single particle analysis, Quick freeze replica electron microscopy, Electron tomography.

ABSTRACT

Spiroplasma, which are known pathogens and commensals of arthropods and plants, are helical-shaped bacteria that lack a peptidoglycan layer. *Spiroplasma* swim by alternating between left- and right-handed helicity. Of note, this system is not related to flagellar

motility, which is widespread in bacteria. A helical ribbon running along the inner side of the helical cell should be responsible for cell helicity and comprises the bacterial actin homolog, MreB, and a protein specific to *Spiroplasma*, fibril. Here, we isolated the ribbon and its major component, fibril filament, for electron microscopy (EM) analysis. Single-particle analysis of the fibril filaments using the negative-staining EM revealed a three-dimensional chain structure composed of rings with a size of 11 nm wide and 6 nm long, connected by a backbone cylinder with an 8.7 nm interval with a twist along the filament axis. This structure was verified through EM tomography of quick-freeze deep-etch replica sample, with a focus on its handedness. The handedness and pitch of the helix for the isolated ribbon and fibril filament agreed with those of the cell in the resting state. Structures corresponding to the alternative state were not identified. These results suggest that the helical cell structure is supported by fibril filaments; however, the helical switch is caused by the force generated by the MreB proteins. The isolation and structural outline of the fibril filaments provide crucial information for an in-depth clarification of the unique swimming mechanism of *Spiroplasma*.

1 Introduction

Mollicutes, which are parasitic or commensal bacteria, evolved from the phylum, Firmicutes, including *Bacillus* and *Clostridium* by reducing their genome size (Razin et al., 1998;Razin and Hayflick, 2010;Grosjean et al., 2014;Miyata et al., 2020). During the course of evolution, the cells became softer and smaller owing to the loss of the peptidoglycan layer. These changes may have allowed some species to transmit their internal housekeeping activities, such as the rotation of ATP synthesis to the outside, resulting in the acquisition of at least three unique motility mechanisms (Relich et al., 2009;Miyata and Hamaguchi, 2016a;b;Distelhorst et al., 2017;Miyata et al., 2020;Toyonaga et al., 2021). Two of the three well studied mechanisms are exerted by *Mycoplasma mobile* and *Mycoplasma pneumoniae*. These species exhibit gliding motilities on solid surfaces, in which leg structures repeatedly catch sialylated oligosaccharides on host cells based on two mechanisms (Miyata, 2010;Miyata and Hamaguchi, 2016a;b). Another motility system is the helicity-switching swimming of *Spiroplasma*, which is the subject of the present study (Movie_S1) (Shaevitz et al.,

2005;Wada and Netz, 2009;Harne et al., 2020b;Sasajima and Miyata, 2021). *Spiroplasma* species are parasitic to plants and arthropods and are characterized as polarized helical-shaped cells with one tapered end (Gasparich, 2002;Harumoto and Lemaitre, 2018;Harne et al., 2020b). These species exhibit obvious chemotaxis despite the absence of genes for the two-component regulatory system in the genome, which is generally responsible for bacterial chemotaxis (Liu et al., 2017). In general, swimming bacteria, including spirochetes, can migrate through the rotational motion of the flagellar motor fixed to the peptidoglycan layer, whereas *Spiroplasma* has a unique swimming system in which kinks propagate along the cell body with a switch between left- and right-handed cell helicity (Fig. 1A). The outline of this mechanism has been clarified as follows. The rotation of helical cells linked to the helicity switch pushes the water back (Trachtenberg and Gilad, 2001;Trachtenberg et al., 2003b;Kürner et al., 2005;Shaevitz et al., 2005;Wada and Netz, 2009;Sasajima and Miyata, 2021). The helicity might be dominated by an intracellular structure called the "ribbon," which localizes along the innermost line of the helical cell structure and is composed of protofilaments. Based on structural studies, ribbons may switch their helicity through changes in the protofilament length (Trachtenberg and Gilad, 2001;Kürner et al., 2005;Cohen-Krausz et al., 2011). Ribbons are known to be composed of fibril proteins specific for *Spiroplasma* species and some *Spiroplasma* MreB (SMreB) proteins related to MreB that are common in rod-shaped bacteria. Although fibril filaments are featured by repetitive ring structures, nanometer-order three-dimensional structure has not been clarified (Trachtenberg and Gilad, 2001;Trachtenberg et al., 2003a;Kürner et al., 2005;Trachtenberg et al., 2008;Cohen-Krausz et al., 2011;Liu et al., 2017).

In the present study, we isolated the filament of fibrils, the major component protein of ribbons and clarified its nanometer-order three-dimensional structure using electron microscopy (EM) and image analyses. The fibril filament has a repetitive structure featuring a ring and a cylinder with a helical pitch similar to those of the ribbon and cell.

2 Materials and Methods

2.1 Bacterial strains and culture conditions

The type strain, TDA-040725-5^{T}, of *Spiroplasma eriocheiris* was cultured in R2 medium

87 (2.5% [wt/vol] heart infusion broth, 8% sucrose, and 10% horse serum) at 30 °C until an
88 optical density of 0.06 to 0.1 was achieved at 600 nm (Liu et al., 2017;Terahara et al.,
89 2017).
90

91 **2.2 Optical microscopy**

92 Cultured cells were centrifuged at 11 000 × *g*, 10 °C for 10 min and suspended in PBS
93 consisting of 75 mM sodium phosphate [pH 7.3], 100 mM NaCl containing 20 mM
94 glucose, and 0.6% methylcellulose, to achieve a cell density 10-fold higher than that of
95 the original (Liu et al., 2017;Terahara et al., 2017). Cells were inserted into a tunnel
96 chamber assembled by taping coverslips, as previously described, and observed under an
97 IX71 microscope (Olympus, Tokyo, Japan) (Uenoyama et al., 2004). A video was
98 captured using a DMK33UX174 complementary metal–oxide–semiconductor (CMOS)
99 camera (The Imaging Source, Taipei, Taiwan) and analyzed using ImageJ v1.53a
100 (https://imagej.nih.gov/ij/).
101

102 **2.3 Electron microscopy**

103 To observe the intact cells, the cell suspension was placed on a hydrophilized grid, fixed
104 using 2% glutaraldehyde, washed with water, and stained with 2% uranyl acetate. To
105 observe the internal structure, the cell suspension on a grid was treated with PBS
106 containing 0.1 mg/mL DNase and 1 mM $MgCl_2$ for 20 s, washed, and stained with 2%
107 uranyl acetate. QFDE-EM was performed as previously reported for specimens
108 suspended in a solution, 10 mM HEPES (pH 7.6), and 150 mM NaCl containing mica
109 flakes (Tulum et al., 2019). The Triton X-100 treatment was done on glass surface before
110 freezing, to observe the internal structure. Images were acquired using a JEM1010 EM
111 (JEOL, Akishima, Japan) equipped with a FastScan-F214(T) charge-coupled device
112 (CCD) camera (TVIPS, Gauting, Germany) and analyzed using ImageJ v1.53a. For
113 tomography, images were captured using a Talos F200C EM (FEI, Eindhoven,
114 Netherlands) equipped with a 4k × 4 K Ceta CMOS camera (FEI). Single-axis tilt series
115 were collected covering an angular range from -50° to +50° with 1.5° steps and analyzed
116 using IMOD (ver 4.11) and PEET (ver 1.15.0).
117

118 **2.4 Isolation of the ribbon and fibril**

119 To isolate the internal structure, 10 mL of cell suspension in PBS was treated with 1%
120 Triton X-100, 0.1 mg/mL DNase, 1 mM $MgCl_2$, and 0.1 mM PMSF, with shaking for 10
121 min at 4 °C. The insoluble fraction was recovered via centrifugation at 20 000 × *g* for 30
122 min at 4 °C, and suspended in PBS to obtain a final volume of 0.2 mL. The sample was
123 placed at the top of sucrose solution layers of 0%, 20%, 30%, 40%, 50%, and 60%, and
124 centrifuged at 20 000 × *g* for 20 min at 4 °C in a 1.5 mL tube at a fixed angle. To isolate
125 the fibril filament, the insoluble fraction was additionally treated with a solution
126 consisting of 2% cholic acid, 20 mM Tris-Cl pH 8.0, 150 mM NaCl at 4 °C for 8 h, and
127 subjected to stepwise density gradient centrifugation. SDS-PAGE and peptide mass
128 fingerprinting were performed as described previously (Nakane and Miyata,
129 2007;Kawakita et al., 2016;Liu et al., 2017). Band intensities were calculated using
130 ImageJ, from scanned gel images.

131

132 **2.5 Preparation of the single-stranded fibril filament**

133 The isolated fibril was adjusted to 1 mg/mL in 20 mM Tris-Cl pH 8.0 and 150 mM NaCl.
134 The fibril suspension (1 mL in a 1.5 mL test tube) was treated on ice for 5 s using a
135 sonicator (UR-21P, TOMY, Tokyo, Japan). The condition of the fibril filament was
136 checked via negative-staining electron microscopy (EM). The processes of sonication and
137 observation were repeated with the fibril suspension until more than 90% of the filaments
138 became single-stranded.

139

140 **2.6 Reconstitution of the 3D structure**

141 The contrast transfer function (CTF) parameters for negative-staining EM images were
142 estimated using the Gctf25 software (Zhang, 2016). The images of fibril filaments were
143 selected automatically using RELION 3.0 (Zivanov et al., 2018) as helical objects and
144 segmented as squares of 200 × 200 pixels with a 90% overlap. These 14,543 images were
145 2D-classified and 11,867 images were selected for further analyses. *Ab-initio*
146 reconstitution was performed using cisTEM (Grant et al., 2018) based on segmented
147 images from 12 classes. The selected 11,867 particle images were 3D-classified using the
148 3D map in RELION 3.0 (Zivanov et al., 2018).

149

150 # 3 Results

151 ## 3.1 Cell helicity is derived from the internal ribbon structure

152 To clarify the relationship between the helical cell morphology and the internal ribbon
153 structure, we first measured the helical pitches of the swimming cells using optical
154 microscopy. Under phase-contrast microscopy, the helical shape of the cells can be
155 observed as a series of dense segments in the defocused image plane relative to the cell
156 axis (Fig. 1A). We measured the pitches along the cell axis for the segments of left and
157 right handedness (Fig. 1F). The helical pitches were 709 ± 74 (n = 50) and 718 ± 65 nm
158 (n = 50) for the left- and right-handed segments, respectively.

159 EM was subsequently employed to analyze the internal ribbon structure and compare
160 the helical pitches of the cells and ribbons. Negative-staining EM revealed images of
161 helical-shaped cells with a narrow tip on one side (Fig. 1B).

162 The internal ribbon structure was exposed by treating the cells with 0.1% Triton X-
163 100 on the grid (Fig. 1C). The ribbon had a "helical" flat structure. These observations
164 are consistent with those of previous studies (Trachtenberg and Gilad, 2001). Thereafter,
165 the pitches of the cell and the exposed ribbon were measured (Fig. 1F). Generally, the
166 specimens for negative-staining EM are placed in vacuum and dried, which can result in
167 distortions and is disadvantageous for evaluating the helicity. We therefore applied quick-
168 freeze, deep-etch (QFDE) EM to visualize the structure in a state as closely as possible to
169 the original (Heuser, 2011). In QFDE, a sample is frozen in milliseconds and exposed by
170 fracturing and etching. Thereafter, a platinum replica was created by shadowing. The
171 observation of the replica by transmission EM provides images with high contrast and
172 resolution, which is markedly better than that provided by conventional scanning electron
173 microscopy (SEM) (Heuser, 2011;Tulum et al., 2019). Replicas were then prepared by
174 fracturing and platinum coating. QFDE-EM revealed cell morphology consistent with
175 that obtained using negative-staining EM (Fig. 1D). Using QFDE-EM, we observed the
176 ribbons exposed to 0.1% Triton X-100 treatment (Fig. 1E). The ribbon had a structure in
177 which the twisted positions were assembled in a line, showing that the images observed
178 by negative-staining EM were flattened. Interestingly, all ribbons were left-handed (Fig.
179 1D, E). When the cells were starved in phosphate-buffered saline (PBS) without glucose

180 for 30 min, they showed a left-handed helix with the same pitch. Therefore, this structure
181 was assumed to be the default state of the cell, and the ribbon switched to the default
182 structure during the visualization process. The helical pitches of the cells and ribbons
183 aligned well with each other, indicating that the ribbon has a critical role for cell helicity
184 (Fig. 1F, Table 1).
185

186 **3.2 Isolation and characterization of the ribbon**

187 For further characterization, we isolated the internal ribbon structure. The cell suspension
188 was treated with 1% Triton X-100 and subjected to stepwise gradient centrifugation with
189 0%, 20%, 30%, 40%, 50%, and 60% sucrose layers. After centrifugation, we found a
190 dense layer of cell contents at the bottom of the 40% sucrose layer. The fraction was
191 recovered and then observed by EM. Based on the observation, the ribbon was found to
192 comprise protofilaments with a width of 66 ± 12 nm (n=20) and a length longer than 2
193 μm, which may correspond to the full length of the cell (Fig. 2A). To analyze the number
194 and width of the protofilaments involved in the isolated ribbon, we traced a cross
195 sectional image profile of the ribbon (Fig. 2D a). Six to nine protofilaments were
196 detected, with peak distances ranging between 4 and 16 nm (Fig. 2D b, c), consistent with
197 the findings of the previous studies (Trachtenberg and Gilad, 2001;Liu et al., 2017).
198 Ribbon twists are observed as periodic frays in the ribbons. The ribbon pitches were
199 measured from the frays as 350 ± 17 nm (n = 47) (Fig. 2D d), which is comparable to the
200 helical pitches of the cells and the ribbons exposed from cells on grids (Fig. 1, Table 1)
201 ($P = 0.7 > 0.01$). SDS-PAGE and peptide mass fingerprinting analyses of this fraction
202 revealed five protein bands, including six proteins (Fig. 2B, Table 2, Table S1). Band (v)
203 contains SMreBs 2 and 4. The whole ribbon fraction mainly comprised the fibril protein
204 (band iii) and a protein mixture of SMreBs 2 and 4 (band v), with an intensity ratio of
205 47% and 37% of the total protein amount, respectively. Further studies are necessary to
206 conclude physical interactions of SPE-1201 and FtsH to fibril protein, because these
207 proteins are abundant in *S eriocheiris* cells (Liu et al., 2017).
208 We intended to use A22, an inhibitor of MreB polymerization, to examine the role of
209 SMreBs in ribbon formation (Shi et al., 2018); this is because the binding of A22 to
210 SMreBs has been suggested from amino acid sequences (Takahashi et al., 2020). First,

211 the effect of 1 mM A22 on the swimming *Spiroplasma* cells was determined. The cells
212 lost their original shape and stopped moving within 2 min (Fig. 2C), suggesting that the
213 functions of SMreBs were inhibited by A22. Thereafter, we isolated the ribbon from cells
214 maintained in 1 mM A22 for 2.5 h at 30 °C. The ribbons were found to be dispersed (Fig.
215 2A, c). SDS-PAGE analysis revealed contents of 67% and 11% for fibril (band iii) and
216 SMreB2 (band v) proteins, respectively (Fig. 2B), suggesting that the protofilaments
217 comprising fibril proteins are stabilized and modified by SMreBs in the ribbon structure.
218

219 **3.3 Isolation and helical pitch of the fibril filament**

220 To analyze the detailed structure of fibril filaments, we treated the ribbon fraction with
221 cholic acid and isolated fibril proteins using sucrose-gradient centrifugation. SDS-PAGE
222 analysis showed that the fraction only contained fibril protein (Fig. 3A). Negative-
223 staining EM revealed that the fibril protein formed filaments that included single-,
224 double-, and more-stranded filaments, suggesting various types of interactions between
225 the fibril protein molecules (Fig. 3B a). A single-stranded fibril filament consisted of
226 repeated ring units with approximately 9 nm intervals (Fig. 3B b c), consistent with
227 previous studies (Townsend et al., 1980;Williamson et al., 1991;Trachtenberg and Gilad,
228 2001;Liu et al., 2017). The ring units were connected by the backbone cylinder (Fig. 3B
229 c). The double-stranded fibril filament appeared to be formed via the alignment of two
230 single-stranded filaments contacting with each other at the ring side not the cylinder side,
231 resulting in a thickness of 14 nm, double that of the single-stranded filament (7 nm) (Fig.
232 3B d e). We analyzed the helical pitches for the double-stranded fibril filaments as the
233 double-stranded fibril filament had a sufficient length of stable helix to cover the pitch,
234 with a clear twist of the ring pattern along the filament axis. Images of the fibril filament
235 cropped from the electron micrographs using the straightening selection tool of the
236 ImageJ software were subjected to Fourier filtering to remove noise (Fig. 3C). However,
237 the handedness of the fibril filament could not be concluded as the negative-staining EM
238 images are projections of the object, and the alignment of the filament on the EM grid
239 was not distinguishable. Therefore, we analyzed the isolated fibril filament using QFDE-
240 EM (Fig. 3D) as the replica synthesized with platinum covers only one side of the object
241 surface. The structures shared features with those from the negative-staining EM (Fig.

3D, Fig. S1). We succeeded in determining their handedness (Fig. 3D a–f) and concluded that the double-stranded fibril filament formed a left-handed helix. The half pitch was distributed at 351 ± 33 nm (n = 50), which aligns with the results of negative-staining EM (Fig. 3E). The agreement of helix pitches in the cell, isolated ribbon, and fibril filament suggests that the fibril filament is a major component of ribbon formation and cell helicity (Table 1).

3.4 Three-dimensional reconstruction of the fibril filaments

To clarify the fibril filament from a three-dimensional (3D) viewpoint, a single-particle analysis was performed on negative-staining EM images. The double-stranded fibril filament was not suitable for image averaging, which might be due to the positional variation in the binding of the two filaments (Fig. 3 and Fig. S2). Therefore, we sonicated the purified fibril fraction to increase the proportion of single-stranded filament and successfully acquired single-stranded images (Fig. 4A). From the selected 11,867 particles with good quality, the 2D-averaged images were classified into three types: (i), (ii), and (iii) (Fig. 4A b). The initial 3D image was reconstructed using the *ab-initio* 3D function of cisTEM software (Grant et al., 2018), and used as the reference for the subsequent 3D classification (Fig. 4A c). 3D structures of the fibril filament reconstructed from 11,867 particles using RELION 3.0 revealed three different conformations (i.e., class 1, left-handed mainly straight (49%); class 2, left-handed with curvature (24%); and class 3, right-handed with curvature (27%) (Fig. 4A d and Fig. S3). The class 1 structure reconstituted with rotational symmetry (C2) was not significantly different from that without symmetry (C1), suggesting that the fibril filament had rotational symmetry without polarity (Fig. S3). We therefore reconstructed the structures of the fibril filaments with C2 symmetry. The 2D reprojections from these three structures corresponded well with the 2D class averages, indicating the validity of the obtained 3D structures (Fig. S3). The 3D structure of the fibril filament had repeating elliptical rings with a pitch of 8.7 nm along the filament axis, and the ring size was 11 wide and 6 nm long along the filament. A short backbone cylinder tilted slightly to the right was found to connect the ring units, resulting in a positive curvature (Fig. 4A d). These characteristics were common to all three classes.

Although the superimposition of class 1 and others showed their structural diffferences, the positions responsible for the differences could not be identified owing to the low resolution of the structures (Fig. 4B). The fibril filaments of all classes were twisted along the filament axis, but with different rotational angles (Fig. S4). The twisting angles were estimated from the angle averages of the first and fourth units, as 5.9 (left-handed), 7.3 (left-handed), and 9.7 (right-handed) degrees for classes 1, 2, and 3, respectively. The twisting angles were estimated from the subunit numbers in the double-stranded images (Fig. 3) for negative-staining and QFDE-EM as 4.9 °and 4.7 °, respectively. These numbers slightly differed from those obtained from the reconstituted 3D structures, suggesting conformational differences between the curved and straight filament forms. These structures can explain the peak distance observed in the density profile of the isolated ribbon (Fig. 2D c, S5).

We proceeded to examine the variation in the ring interval (Fig. 4C, Fig. S6). 2D averaged images were measured for 60 ring intervals. The intervals were 8.86 ± 0.24 nm (n=60) and did not show group separation, suggesting that the intervals do not have clear conformational change, despite some having an elasticity up to 2.7%.

3.5 Handedness verified based on the tomography of the QFDE replica

The 3D images reconstituted from negative-staining EM had common features, despite variations in curvature and twist. The reconstructed structures all have rings and cylinders tilted slightly to the right along the filament axis when viewed from the front and back sides, respectively (Fig. 4A d), indicating that the three classes belong to the same side of mirror images. As the images by negative-staining EM are projections of the objects, the reconstituted structures may mirror images of the real structures. Thereafter, we intended to verify the handedness of the reconstituted structures by EM tomography of the QFDE replica sample (Fig. 5); this is because the tomogram cannot be a mirror image (Briegel et al., 2013;Jensen, 2015).

We made QFDE replicas from the fraction containing single-stranded fibril filaments, acquired images every 1.5° to 50° specimen tilt for both directions, reconstituted tomograms (Movie_S4) (Fig. 5A), and then obtained a structure by averaging 60 subtomograms (Fig. 5B). As expected, the resulting filament structure had

304 rings and cylinders. The rings and cylinders were tilted from the filament axis, rising to
305 the right from the horizontal axis by 4–5 ° and 74–82 ° when viewed from the front and
306 back, respectively (Fig. 5C and S7), which align well with the features of structures from
307 negative-staining EM. These results indicate that the classes of structures from negative-
308 staining EM had the same handedness as the real structures (Fig. 5C).
309

310 **4 Discussion**

311 **4.1 Structures of the isolated fibril**

312 The unique swimming of *Spiroplasma* is believed to be caused by the ribbon structure
313 (Kürner et al., 2005;Cohen-Krausz et al., 2011;Harne et al., 2020b;Sasajima and Miyata,
314 2021). In this study, we isolated filaments of fibrils, the major protein of the ribbon, and
315 revealed the 3D structure of the single-stranded filament at the nanometer scale using
316 EM. Fibril filaments have been isolated for a long time, and their EM images show a
317 characteristic ring repeat structure with a high contrast (Townsend et al.,
318 1980;Williamson et al., 1991;Trachtenberg and Gilad, 2001;Trachtenberg et al.,
319 2003a;Cohen-Krausz et al., 2011;Liu et al., 2017). However, a nanometer-order three-
320 dimensional fibril filament structure is yet to be revealed. Sonication during the isolation
321 process was effective in isolating the single-stranded filament, whose uniform structure
322 was advantageous for image averaging (Fig. 3). Negative-staining EM was used to
323 reconstruct the structure (Fig. 4). However, as this method produces projection images,
324 the handedness of the reconstructed structure may be incorrect. Therefore, we confirmed
325 the handedness of the structure by tomographic analysis of platinum replicas prepared by
326 QFDE-EM (Fig. 5). The final structure was a repeating structure of elliptical rings
327 connected by backbone cylinders aligned off-axis with a gentle left-handed helix, which
328 is consistent with that of previous studies. No polarity was observed in the filament
329 structure.

330 These results raise questions regarding the alignment of the 512 amino acid residues
331 of the fibril protein with the structure and the structure formed by the 1-228 amino acid
332 residues possessing obvious sequence similarity to methylthioadenosine/S-
333 adenosylhomocysteine (MTA/SAH) nucleosidase (Cohen-Krausz et al., 2011;Parveen

334 and Cornell, 2011;Sasajima and Miyata, 2021). These questions will be answered via
335 cryo-EM analysis of the single-stranded fibril filaments prepared in this study.
336

337 **4.2 Ribbon structure in the cell**

338 When *Spiroplasma* cells were lysed with a detergent, the ribbon structure appeared to run
339 along the entire length of the cell axis (Fig. 1) (Trachtenberg and Gilad, 2001). In this
340 study, we isolated ribbons with a length equivalent with the entire length of the cell (Fig.
341 2). These observations suggest that the ribbon is a relatively stable structure rather than a
342 highly dynamic one that disappears in a short time. Furthermore, as the extraction
343 procedure with cholic acid yielded a structure consisting only of fibril filaments (Fig. 3),
344 the stable properties of the ribbon are likely to be derived from the fibril filament. The
345 helix of the fibril filament was directly observed in the double-stranded filament (Fig. 3).
346 The constant helical pitch of a single strand could not be detected, which may be due to
347 its irregular attachment to the EM grid. The two strands of double-stranded filaments may
348 stabilize the inherent helical character of the filament by combining them. The
349 handedness and pitch observed in the duplexes were left-handed and 351±34 (702±68)
350 nm, respectively, aligning with the helical character of the cells at rest (Fig. 1, 3). As
351 previous observations revealed the presence of ribbons in the innermost portion of the
352 cell helix (Kürner et al., 2005;Trachtenberg et al., 2008), the helix of the resting cell
353 should directly reflect the characteristics of the fibril filament.

354 During swimming, the cell switches its helical form into a right-handed one with a
355 helical pitch similar to the left-handed one (Fig. 1). However, we could not find the
356 corresponding right-handed helical structures in the isolated fibril filaments or ribbons.
357 Only class 3 3D image reconstructed from 27% of the negative-staining EM images
358 suggested a right-handed helical structure (Fig. 4); however, a further investigation is
359 needed to conclude that this structure is stable one as the protein can be distorted by
360 sticking to the EM grid in this analysis. These observations suggest that the right-handed
361 helical structure observed in cells during swimming does not originate from another
362 stable fibril filament structure (Fig. 4). The helix switch can also be explained by
363 assuming that two types of filaments running parallel to the ribbon are alternately
364 extended and contracted (Kürner et al., 2005;Cohen-Krausz et al., 2011). To test this

365 notion, we examined the distribution of the fibril filament lengths and found that the
366 length distribution had a single peak at 8.86 ± 0.24 nm (Fig. 4). Such finding suggests
367 that the fibril filament has only one stable length and does not support a helical switch
368 caused by a length change in the fibril filament.
369

370 **4.3 Role of fibril in the swimming mechanism**

371 The fibril protein is conserved in most *Spiroplasma* species with high amino acid
372 sequence similarity (Ku et al., 2014). However, *Spiroplasma sabaudiense* and
373 *Spiroplasma helicoide* do not contain fibril proteins, despite exhibiting helicity-switching
374 swimming (Harne et al., 2020b). Recently, the expression of two SMreB proteins in the
375 non-swimming synthetic bacterium, syn3.0B, was demonstrated to reproduce cell helicity
376 and helicity-switching swimming (Hutchison et al., 2016; Kiyama et al., 2021).
377 Moreover, the expression of SMreB induced cell helicity and its switching in spherical
378 Mollicutes species (Lartigue et al., 2021), implying that the helix formation of the cell
379 and the force generation for switching are caused by SMreBs. Then, what is the role of
380 fibril filaments in most *Spiroplasma* species? Isolated MreB binds to fibril filaments
381 (Harne et al., 2020a). Further, our results (Fig. 2) support the binding of SMreB to the
382 fibril filaments. These observations suggest that MreB exerts a force on fibril filaments
383 for swimming. SMreBs might cause helicity-switching swimming, and fibril filaments
384 might be effective at obtaining high energy efficiency and chemotaxis; this is supported
385 by the observation that swimming reconstructed in syn3.0B by SMreBs lacks processivity
386 (Kiyama et al., 2021).
387

388 **5 Conflict of Interest**

389 The authors declare that the research was conducted in the absence of any commercial or
390 financial relationships that could be construed as a potential conflict of interest.
391

392 **6 Author Contributions**

393 YS and MM designed the experiments. YS performed the experiments. YS, TK, TM,
394 AK, and KN acquired and analyzed the images. YS and MM wrote the manuscript. All
395 authors discussed the data.

7 Funding

This study was supported by Grants-in-Aid for Scientific Research A (MEXT KAKENHI, Grant Number JP17H01544), JST CREST (Grant Number JPMJCR19S5), the Osaka City University (OCU) Strategic Research Grant 2017 for top priority research to MM, JSPS KAKENHI (Grant Number JP25000013), the Platform Project for Supporting Drug Discovery and Life Science Research (BINDS) from AMED (Grant Number JP19am0101117 and support number 1282), the Cyclic Innovation for Clinical Empowerment (CiCLE) from AMED (Grant Number JP17pc0101020), and JEOL YOKOGUSHI Research Alliance Laboratories of Osaka University to KN.

8 Acknowledgments

We thank Yuhei O Tahara, Daichi Takahashi, Hana Kiyama, and Ikuko Fujiwara at the Graduate School of Science, Osaka Metropolitan University, Japan, for their helpful discussions.

412 ## REFERENCES

413 Briegel, A., Pilhofer, M., Mastronarde, D.N., and Jensen, G.J. (2013). The challenge of
414 determining handedness in electron tomography and the use of DNA origami
415 gold nanoparticle helices as molecular standards. *J Struct Biol* 183**,** 95-98.
416 Cohen-Krausz, S., Cabahug, P.C., and Trachtenberg, S. (2011). The monomeric,
417 tetrameric, and fibrillar organization of Fib: the dynamic building block of the
418 bacterial linear motor of *Spiroplasma melliferum* BC3. *J Mol Biol* 410**,** 194-213.
419 Distelhorst, S.L., Jurkovic, D.A., Shi, J., Jensen, G.J., and Balish, M.F. (2017). The variable
420 internal structure of the *Mycoplasma penetrans* attachment organelle revealed
421 by biochemical and microscopic analyses: implications for attachment organelle
422 mechanism and evolution. *J Bacteriol* 199.
423 Gasparich, G.E. (2002). *Spiroplasmas*: evolution, adaptation and diversity. *Front Biosci* 7**,**
424 d619-640.
425 Grant, T., Rohou, A., and Grigorieff, N. (2018). cisTEM, user-friendly software for single-
426 particle image processing. *Elife* 7**,** e35383.
427 Grosjean, H., Breton, M., Sirand-Pugnet, P., Tardy, F., Thiaucourt, F., Citti, C., Barre, A.,
428 Yoshizawa, S., Fourmy, D., De Crecy-Lagard, V., and Blanchard, A. (2014).
429 Predicting the minimal translation apparatus: lessons from the reductive
430 evolution of mollicutes. *PLoS Genet* 10**,** e1004363.
431 Harne, S., Duret, S., Pande, V., Bapat, M., Beven, L., and Gayathri, P. (2020a). MreB5 Is a
432 determinant of rod-to-helical transition in the cell-wall-less bacterium
433 *Spiroplasma*. *Curr Biol* 30**,** 4753-4762.e4757.
434 Harne, S., Gayathri, P., and Beven, L. (2020b). Exploring *Spiroplasma* biology:
435 opportunities and challenges. *Front Microbiol* 11**,** 589279.
436 Harumoto, T., and Lemaitre, B. (2018). Male-killing toxin in a bacterial symbiont of
437 *Drosophila*. *Nature* 557**,** 252-255.
438 Heuser, J.E. (2011). The origins and evolution of freeze-etch electron microscopy. *J*
439 *Electron Microsc (Tokyo)* 60 Suppl 1**,** S3-29.
440 Hutchison, C.A., 3rd, Chuang, R.Y., Noskov, V.N., Assad-Garcia, N., Deerinck, T.J.,
441 Ellisman, M.H., Gill, J., Kannan, K., Karas, B.J., Ma, L., Pelletier, J.F., Qi, Z.Q.,
442 Richter, R.A., Strychalski, E.A., Sun, L., Suzuki, Y., Tsvetanova, B., Wise, K.S.,
443 Smith, H.O., Glass, J.I., Merryman, C., Gibson, D.G., and Venter, J.C. (2016).
444 Design and synthesis of a minimal bacterial genome. *Science* 351**,** aad6253.
445 Jensen, G.J. (2015). "Getting started in Cryo-EM with professor Grant Jensen".).
446 Kürner, J., Frangakis, A.S., and Baumeister, W. (2005). Cryo-electron tomography reveals
447 the cytoskeletal structure of *Spiroplasma melliferum*. *Science* 307**,** 436-438.
448 Kawakita, Y., Kinoshita, M., Furukawa, Y., Tulum, I., Tahara, Y.O., Katayama, E., Namba,
449 K., and Miyata, M. (2016). Structural study of MPN387, an esssential protein for
450 gliding motility of a human-pathogenic bacterium, *Mycoplasma pneumoniae*. *J*
451 *Bacteriol* 198**,** 2352-2359.
452 Kiyama, H., Kakizawa, S., Sasajima, Y., Tahara, Y.O., and Miyata, M. (2021).
453 Reconstitution of minimal motility system based on *Spiroplasma* swimming by
454 expressing two bacterial actins in synthetic minimal bacterium. *bioRxiv*.

455 Ku, C., Lo, W.S., and Kuo, C.H. (2014). Molecular evolution of the actin-like MreB protein
456 gene family in wall-less bacteria. *Biochem Biophys Res Commun* 446**,** 927-932.
457 Lartigue, C., Lambert, B., Rideau1, F., Decossas, M., Hillion, M., Douliez, J.-P., Hardouin,
458 J., Lambert, O., Blanchard, A., and Béven, L. (2021). Tuning spherical cells into
459 kinking helices in wall-less bacteria. *bioRxiv*.
460 Liu, P., Zheng, H., Meng, Q., Terahara, N., Gu, W., Wang, S., Zhao, G., Nakane, D., Wang,
461 W., and Miyata, M. (2017). Chemotaxis without conventional two-component
462 system, based on cell polarity and aerobic conditions in helicity-switching
463 swimming of *Spiroplasma eriocheiris*. *Front Microbiol* 8**,** 58.
464 Miyata, M. (2010). Unique centipede mechanism of *Mycoplasma* gliding. *Annu Rev*
465 *Microbiol* 64**,** 519-537.
466 Miyata, M., and Hamaguchi, T. (2016a). Integrated information and prospects for gliding
467 mechanism of the pathogenic bacterium *Mycoplasma pneumoniae*. *Front*
468 *Microbiol* 7**,** 960.
469 Miyata, M., and Hamaguchi, T. (2016b). Prospects for the gliding mechanism of
470 *Mycoplasma mobile*. *Curr Opin Microbiol* 29**,** 15-21.
471 Miyata, M., Robinson, R.C., Uyeda, T.Q.P., Fukumori, Y., Fukushima, S.I., Haruta, S.,
472 Homma, M., Inaba, K., Ito, M., Kaito, C., Kato, K., Kenri, T., Kinosita, Y., Kojima, S.,
473 Minamino, T., Mori, H., Nakamura, S., Nakane, D., Nakayama, K., Nishiyama, M.,
474 Shibata, S., Shimabukuro, K., Tamakoshi, M., Taoka, A., Tashiro, Y., Tulum, I.,
475 Wada, H., and Wakabayashi, K.I. (2020). Tree of motility - A proposed history of
476 motility systems in the tree of life. *Genes Cells* 25**,** 6-21.
477 Nakane, D., and Miyata, M. (2007). Cytoskeletal "jellyfish" structure of *Mycoplasma*
478 *mobile*. *Proc Natl Acad Sci U S A* 104**,** 19518-19523.
479 Parveen, N., and Cornell, K.A. (2011). Methylthioadenosine/S-adenosylhomocysteine
480 nucleosidase, a critical enzyme for bacterial metabolism. *Mol Microbiol* 79**,** 7-20.
481 Razin, S., and Hayflick, L. (2010). Highlights of mycoplasma research--an historical
482 perspective. *Biologicals* 38**,** 183-190.
483 Razin, S., Yogev, D., and Naot, Y. (1998). Molecular biology and pathogenicity of
484 mycoplasmas. *Microbiol Mol Biol Rev* 62**,** 1094-1156.
485 Relich, R.F., Friedberg, A.J., and Balish, M.F. (2009). Novel cellular organization in a
486 gliding mycoplasma, Mycoplasma insons. *J Bacteriol* 191**,** 5312-5314.
487 Sasajima, Y., and Miyata, M. (2021). Prospects for the mechanism of *Spiroplasma*
488 swimming. *Front Microbiol* 12**,** 706426.
489 Shaevitz, J.W., Lee, J.Y., and Fletcher, D.A. (2005). *Spiroplasma* swim by a processive
490 change in body helicity. *Cell* 122**,** 941-945.
491 Shi, H., Bratton, B.P., Gitai, Z., and Huang, K.C. (2018). How to build a bacterial cell:
492 MreB as the foreman of *E. coli* construction. *Cell* 172**,** 1294-1305.
493 Takahashi, D., Fujiwara, I., and Miyata, M. (2020). Phylogenetic origin and sequence
494 features of MreB from the wall-less swimming bacteria *Spiroplasma*. *Biochem*
495 *Biophys Res Commun* 533**,** 638-644.

Terahara, N., Tulum, I., and Miyata, M. (2017). Transformation of crustacean pathogenic bacterium *Spiroplasma eriocheiris* and expression of yellow fluorescent protein. *Biochem Biophys Res Commun* 487**,** 488-493.

Townsend, R., Archer, D.B., and Plaskitt, K.A. (1980). Purification and preliminary characterization of *Spiroplasma* fibrils. *J Bacteriol* 142**,** 694-700.

Toyonaga, T., Kato, T., Kawamoto, A., Kodera, N., Hamaguchi, T., Tahara, Y.O., Ando, T., Namba, K., and Miyata, M. (2021). Chained structure of dimeric F_1-like ATPase in *Mycoplasma mobile* gliding machinery. *mBio***,** e0141421.

Trachtenberg, S., Andrews, S.B., and Leapman, R.D. (2003a). Mass distribution and spatial organization of the linear bacterial motor of *Spiroplasma citri* R8A2. *J Bacteriol* 185**,** 1987-1994.

Trachtenberg, S., Dorward, L.M., Speransky, V.V., Jaffe, H., Andrews, S.B., and Leapman, R.D. (2008). Structure of the cytoskeleton of *Spiroplasma melliferum* BC3 and its interactions with the cell membrane. *J Mol Biol* 378**,** 778-789.

Trachtenberg, S., and Gilad, R. (2001). A bacterial linear motor: cellular and molecular organization of the contractile cytoskeleton of the helical bacterium *Spiroplasma melliferum* BC3. *Mol Microbiol* 41**,** 827-848.

Trachtenberg, S., Gilad, R., and Geffen, N. (2003b). The bacterial linear motor of *Spiroplasma melliferum* BC3: from single molecules to swimming cells. *Mol Microbiol* 47**,** 671-697.

Tulum, I., Tahara, Y.O., and Miyata, M. (2019). Peptidoglycan layer and disruption processes in *Bacillus subtilis* cells visualized using quick-freeze, deep-etch electron microscopy. *Microscopy (Oxf)* 68**,** 441-449.

Uenoyama, A., Kusumoto, A., and Miyata, M. (2004). Identification of a 349-kilodalton protein (Gli349) responsible for cytadherence and glass binding during gliding of *Mycoplasma mobile*. *J. Bacteriol.* 186**,** 1537-1545.

Wada, H., and Netz, R.R. (2009). Hydrodynamics of helical-shaped bacterial motility. *Phys Rev E Stat Nonlin Soft Matter Phys* 80**,** 021921.

Williamson, D.L., Renaudin, J., and Bove, J.M. (1991). Nucleotide sequence of the *Spiroplasma citri* fibril protein gene. *J Bacteriol* 173**,** 4353-4362.

Zhang, K. (2016). Gctf: Real-time CTF determination and correction. *J Struct Biol* 193**,** 1-12.

Zivanov, J., Nakane, T., Forsberg, B.O., Kimanius, D., Hagen, W.J., Lindahl, E., and Scheres, S.H. (2018). New tools for automated high-resolution cryo-EM structure determination in RELION-3. *Elife* 7**,** e42166.

1 Data Availability Statement

The datasets presented in this study can be found in the Supplementary Material.

535 **Table 1.** Dimensions of the cell and ribbon

Parameters	Negative-staining EM	QFDE-EM	Optical microscopy
Cell helical pitch	706 ± 74 nm 703 nm	711 ± 41 nm (LH) 711 nm (LH)	709 ± 74 nm (LH) 702 nm (LH) 718 ± 65 nm (RH) 711 nm (RH)
Ribbon helical pitch	691 ± 53 nm 700 nm	700 ± 60 nm (LH) 706 nm (LH)	
Isolated ribbon 1/2 helical pitch	350 ± 17 nm 352 nm		
Isolated fibril 1/2 helical pitch	341 ± 27 nm 335 nm	351 ± 34 nm (LH) 352 nm (LH)	

536 Handedness is represented by LH and RH.

537 The upper and lower rows show the mean, standard deviation, and median, respectively.

538

539

540 **Table 2.** Protein components of the ribbon isolated from original cells[1].

Protein Band[1]	Gene ID	Annotation	Mascot Score[2]	Mass (kDa)[3]	Density ratio (%)	
					Original	A22 treated
(i)	SPE-1201	Hypothetical protein	72	85.8	4	5
(ii)	SPE-0013	FtsH	84	77.0	12	17
(iii)	SPE-0666	Fibril	206	58.7	47	67
(iv)	SPE-1231	SMreB5	98	38.5	10	7
(v)	SPE-1224	SMreB2	80	37.8	27	4
	SPE-1230	SMreB4		40.7		

541

542 [1] From A22-treated cells, the proteins common to the original cells were identified for bands (i)–(iv). For band (v) only,
543 SMreB2 was identified.

544 [2] Mascot Score is the logarithm of probability that the observed match is a random event.

545 [3] Calculated from the amino acid sequence as a monoisotopic molecule.

546

547 **Figure Legends**

548 **Figure 1.** Helicity of the cell and ribbon structure. **(A)** Phase-contrast microscopy of
549 swimming cell. The blue and red segments, and broken line indicate the left- and right-
550 handed helicity, and cell axes, respectively. The pitch was measured as indicated by a
551 double headed arrow. **(B, C)** Cell and ribbon images acquired by negative-staining EM.
552 **(D, E)** Cell and ribbon images acquired by QFDE EM. (F) Helical pitches of cells and
553 ribbon measured by optical microscopy, negative-staining EM, and QFDE-EM.
554 Handedness was judged by optical microscopy and QFDE-EM. All cells analyzed by
555 QFDE-EM were left-handed as they were grown under a starved condition.
556

557 **Figure 2.** Isolation and characterization of the ribbon. **(A)** Isolated ribbon structure. (a)
558 The whole structure of the isolated ribbon with helicity as shown by periodical wide
559 positions (marked by arrows). (b) The magnified image of the isolated ribbon and the
560 helical pitch is indicated by a bidirectional arrow. (c) Ribbon fraction isolated from cells
561 treated with A22. **(B)** Protein profiles of the ribbon fraction isolated from cells untreated
562 and treated with A22. **(C)** Cell images before (a) and after (b) treatment with 1 mM A22
563 for 2 min. **(D)** Numerical characterization. (a) Sectional image profile of the area boxed
564 in panel (A b). The peaks correspond to the center of the protofilament. (b) Histogram for
565 the number of protofilaments involved in a ribbon. (c) Histogram for the protofilament
566 width in ribbons. The distribution can be fitted by two Gaussian curves marked (i) and
567 (ii), with peaks around 7.0 and 10.5 nm, respectively. (d) Histogram for the helical
568 pitches of the isolated ribbon, fitted by a Gaussian curve with a peak at 351 ± 16 nm
569 (n=47).
570

571 **Figure 3.** Structures of the isolated fibril filament. **(A)** Protein profiles of the fractions in
572 the purification process for fibril protein. (i) Whole cell lysate. (ii) Supernatant. (iii)
573 Isolated ribbon. The sample amount was adjusted to be delivered from the same cell
574 number. **(B)** Purified fibril filaments observed by negative-staining EM. (a) Field image.
575 White and black arrows indicate typical single and double strands, respectively. (b, c)
576 Front and side views of the single-stranded fibril filament. (d, e) Front and side views of
577 the double-stranded fibril filament. The ring intervals marked by an asterisk were 9 nm

578 for both single and double strands. **(C)** Double-stranded filaments reconstituted through
579 Fourier filtering. **(D)** Fibril filaments observed by QFDE-EM. Field (a) and single-
580 stranded filaments (b, c, d) are presented. The back (b), front (c), and side (d) views are
581 shown. (e) Single-stranded filament. (f, g) Double-stranded filament image (f) was
582 reduced for noise through Fourier filtering. (g). The helical pitch was measured as
583 depicted by a double headed broken arrow. The handedness was clearly observed at the
584 points marked by white arrows in the panel (a) and panel (f) image.
585
586 **Figure 4.** Three-dimensional reconstruction of the fibril filaments. **(A)** Workflow of
587 single particle analysis by negative-staining EM. (a) Field images of single-stranded fibril
588 filaments prepared by sonication. (b) Eight averaged images obtained by a function of 2D
589 classification in RELION software. (c) The initial 3D model generated by a function of
590 *ab-initio* reconstruction in cisTEM software. (d) Three different conformations of the
591 fibril filament reconstituted by a function of 3D refinement in RELION software. **(B)**
592 Superpose of class 1 (left-handed) and class 2 (left-handed) and 3 (right-handed)
593 structures. The fitting reference is indicated by a dashed box. **(C)** Distribution of the ring
594 intervals. Left: Ring intervals in an averaged image with complete rings. Right: Plotted
595 ring intervals.
596
597 **Figure 5.** Comparison of the 3D structures of the fibril filament reconstructed from
598 QFDE and negative-staining EM. **(A)** Replica image of mainly single-stranded fibril
599 filaments. Left: A field image is shown from a tilt series (Movie_S2). Right lower:
600 Magnified images of single fibril filament are shown as a raw image (a), a slice from the
601 tomogram (b), and a subtomogram (c). **(B)** Structure averaged from 60 subtomograms.
602 The leftmost image is presented under different thresholds from other three images. **(C)**
603 Superpose of the 3D structures from single-particle analysis (grey) and subtomogram
604 averaging (magenta). Long axes of ring and cylinder are depicted by broken red arrows.
605 The filament axes were detected by a function "relion_align_symmetry --sym d2" in
606 RELION-3.0.
607

Fig. 1

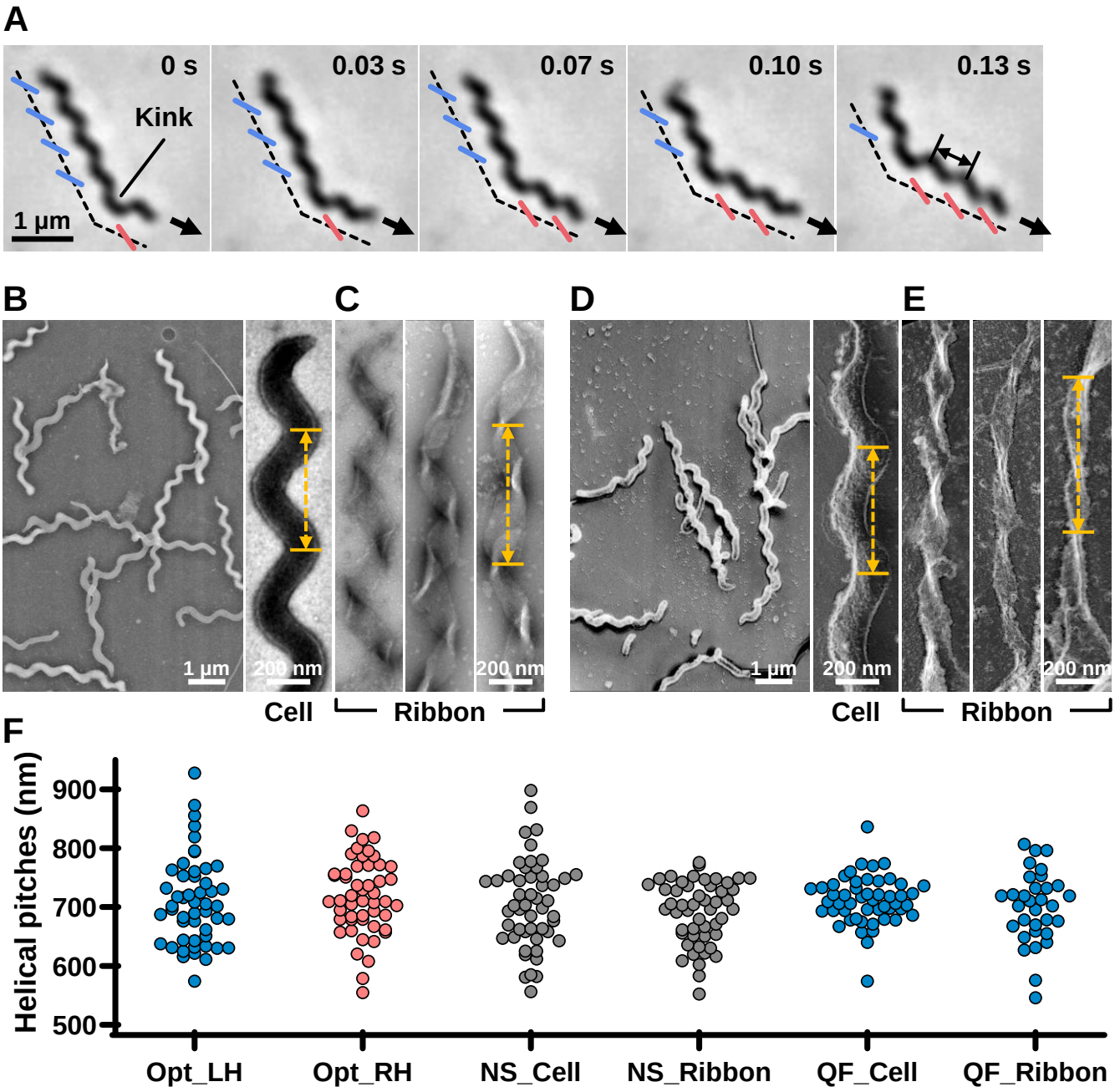
A
0 s
0.03 s
0.07 s
0.10 s
0.13 s
Kink
1 µm
B
C
D
E
1 µm
200 nm
200 nm
1 µm
200 nm
200 nm
Cell
Ribbon
Cell
Ribbon
F
Helical pitches (nm)
900
800
700
600
500
Opt_LH
Opt_RH
NS_Cell
NS_Ribbon
QF_Cell
QF_Ribbon

Fig. 2

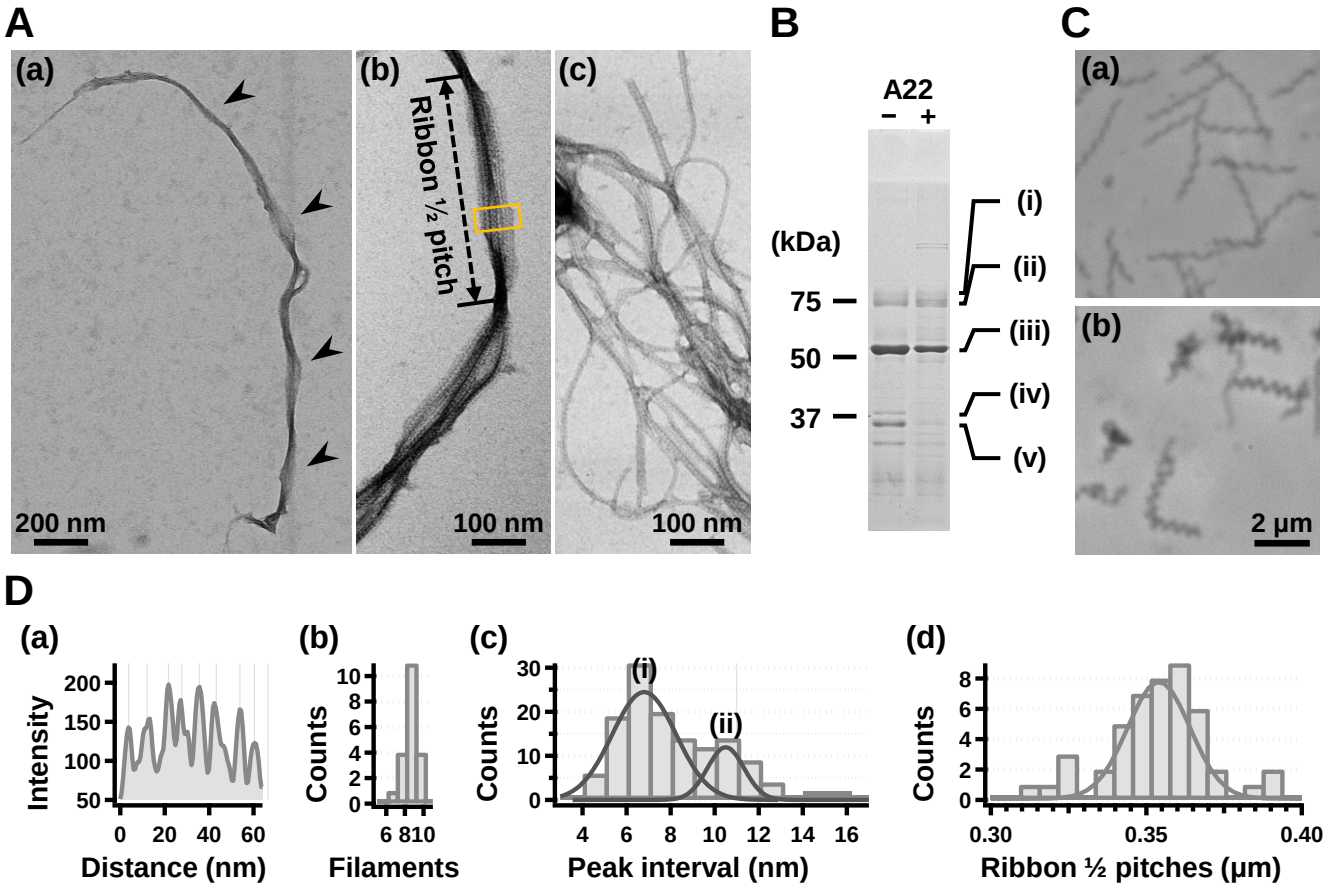
A
(a)
200 nm
(b)
Ribbon ½ pitch
100 nm
(c)
100 nm
B
A22
− +
(kDa)
75
50
37
(i)
(ii)
(iii)
(iv)
(v)
C
(a)
(b)
2 µm
D
(a)
Intensity
200
150
100
50
0 20 40 60
Distance (nm)
(b)
Counts
10
8
6
4
2
0
6 8 10
Filaments
(c)
Counts
30
20
10
0
(i)
(ii)
4 6 8 10 12 14 16
Peak interval (nm)
(d)
Counts
8
6
4
2
0
0.30 0.35 0.40
Ribbon ½ pitches (µm)

Fig. 3

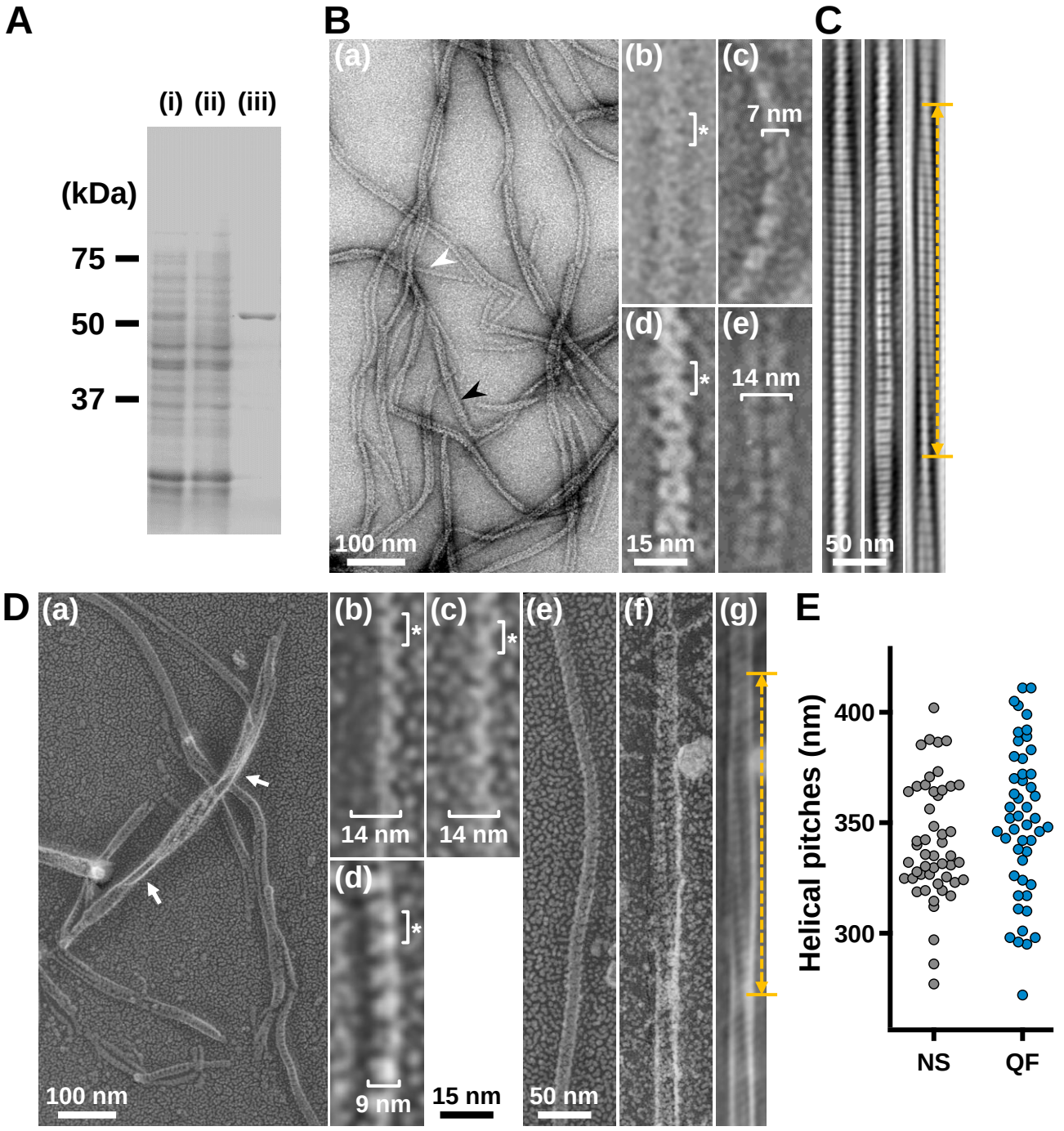
A
(i) (ii) (iii)
(kDa)
75
50
37
B
(a)
100 nm
(b)
(c)
7 nm
(d)
(e)
14 nm
15 nm
C
50 nm
D
(a)
100 nm
(b)
14 nm
(c)
14 nm
(d)
9 nm
15 nm
(e)
(f)
(g)
50 nm
E
Helical pitches (nm)
400
350
300
NS
QF

Fig. 4

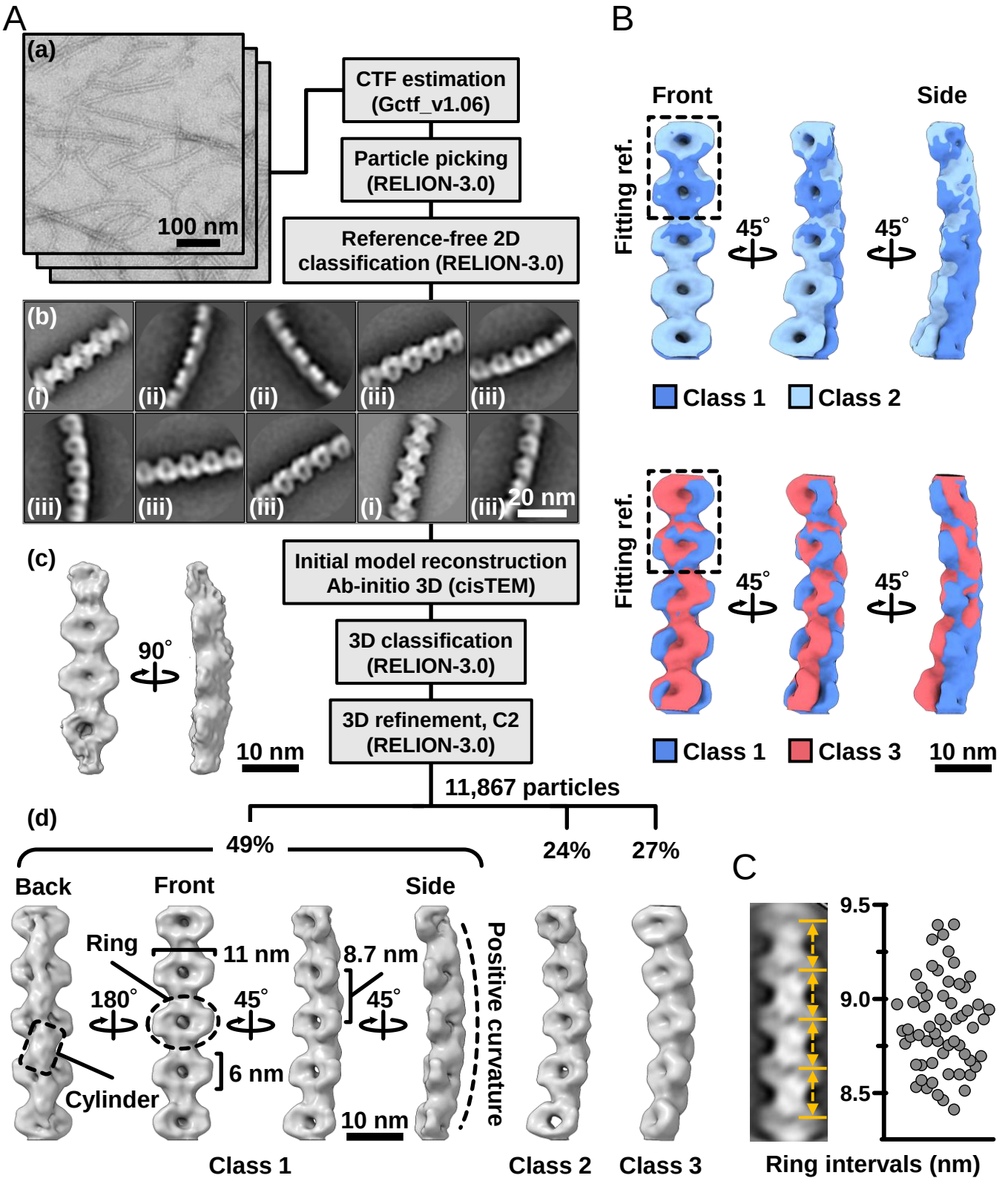
A
(a)
100 nm
CTF estimation (Gctf_v1.06)
Particle picking (RELION-3.0)
Reference-free 2D classification (RELION-3.0)
(b)
(i)
(ii)
(iii)
20 nm
(c)
90°
10 nm
Initial model reconstruction Ab-initio 3D (cisTEM)
3D classification (RELION-3.0)
3D refinement, C2 (RELION-3.0)
11,867 particles
(d)
49%
24%
27%
Back
Front
Side
Ring
11 nm
8.7 nm
180°
45°
6 nm
Cylinder
10 nm
Positive curvature
Class 1
Class 2
Class 3
B
Front
Side
Fitting ref.
45°
Class 1
Class 2
Class 3
10 nm
C
9.5
9.0
8.5
Ring intervals (nm)

Fig. 5

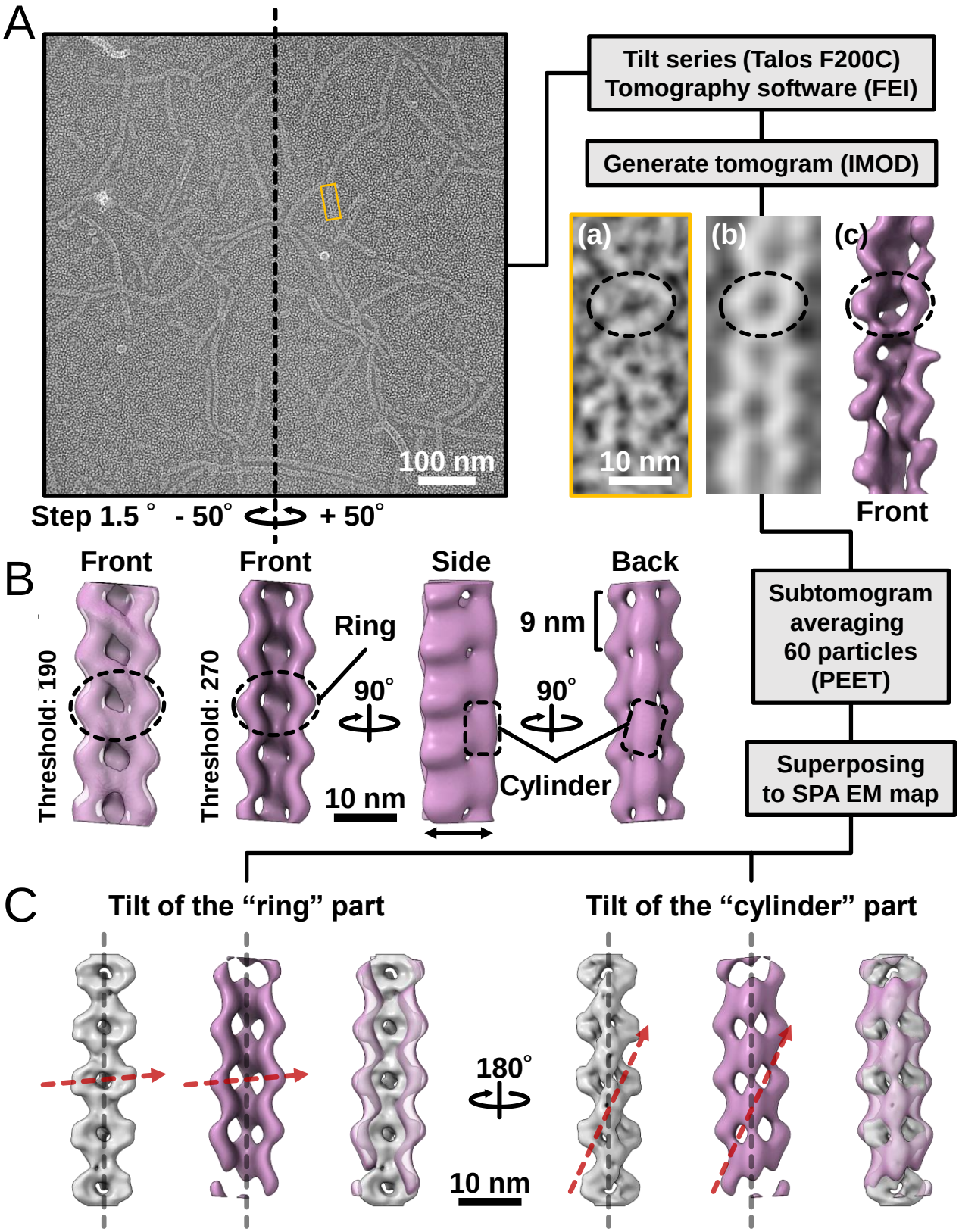
A
100 nm
Step 1.5 °
- 50°
+ 50°
Tilt series (Talos F200C)
Tomography software (FEI)
Generate tomogram (IMOD)
(a)
(b)
(c)
10 nm
Front
B
Front
Front
Side
Back
Threshold: 190
Threshold: 270
Ring
90°
90°
9 nm
10 nm
Cylinder
Subtomogram averaging 60 particles (PEET)
Superposing to SPA EM map
C
Tilt of the "ring" part
Tilt of the "cylinder" part
180°
10 nm